Autonomous Robots (2020) 44:1469–1484
https://doi.org/10.1007/s10514-020-09938-5

Angular momentum-based control of an underactuated orthotic system for crouch-to-stand motion

Curt A. Laubscher[1] · **Ryan J. Farris**[2] · **Jerzy T. Sawicki**[1]

Received: 8 October 2019 / Accepted: 20 July 2020 / Published online: 8 August 2020

Abstract
This paper presents an angular momentum-based controller for crouch-to-stand motion of a powered pediatric lower-limb orthosis. The control law is developed using an underactuated triple pendulum model representing the legs of an orthosis-dummy system where the hip and knee joints are actuated but the ankle joint is unpowered. The control law is conceived to drive the angular momentum of the system to zero, thereby bringing the system to a statically balanced upright configuration. The parameters of the dynamic model of the orthosis-dummy system are experimentally identified and used to synthesize the momentum-based controller. Control parameters are selected using closed-loop pole placement of the linearized system via numerical optimization to ensure local closed-loop stability with adequate damping and satisfactory response time without too large controller gains. The controller is applied in simulation to determine the region of viable initial conditions resulting in no knee hyperextension or loss of balance, as determined from a zero-moment point analysis. The controller is then implemented in experiment showing feasibility of the control strategy in practice. Results are compared against a similarly-synthesized linear-quadratic regulator.

Keywords Underactuated pendulum · Angular momentum-based controller · Crouch-to-stand · Orthosis

1 Introduction

Currently available powered lower-limb orthoses on the market, or described in the literature, such as the Indego (Farris et al. 2011) and ReWalk (Esquenazi et al. 2012) exoskeletons, often require the user to manage balance aids such as crutches, walkers, or hand rails. Other devices such as the Rex exoskeleton (Kwak et al. 2015) manage balance through large platform feet and control which ensures that the center of pressure (CoP) of the system never leaves the area of the foot platform. However, managing balance in this fashion comes with weight, size, and speed penalties. Development of a control law capable of balancing the exoskeleton wearer without the need for balance aids would provide significant benefit to exoskeleton usability and user acceptance.

Given the importance of balance in orthosis-assisted gait, quantitative assessment of whole-system balance continues to be an important area of research. The bulk dynamics of a human-orthosis system can be represented using a robot model, which can derived using, for example, the Newton–Euler method based on first principals from rigid-body dynamics or the Euler–Lagrange method based on principals of energy conservation and dissipation (Craig 2005). A robotic system is balanced when the necessary reaction forces and torques can be provided by the components in contact with the ground. Various criteria are described in the literature which ensure a robotic system remains balanced during operation. Usually, this is done by controlling the system so that some calculated point remains within the support region of the system, defined as the convex hull of the points in contact with the ground. The zero-moment point (ZMP) (Siciliano and Khatib 2008; Vukobratović and Borovac 2004) is a common choice and is defined as the point on the ground where the equivalent horizontal reaction moments are equal to zero. This point coincides with the CoP when the system is balanced and can be computed using the geometry of the robotic

✉ Jerzy T. Sawicki
j.sawicki@csuohio.edu

Curt A. Laubscher
c.laubscher@csuohio.edu

[1] Department of Mechanical Engineering, Cleveland State University, Cleveland, OH, USA

[2] Human Motion and Control Division, Parker Hannifin Corporation, Macedonia, OH, USA

system, inertial properties of the links, and measurements or estimates of the joint positions, velocities, and accelerations. The system is balanced when the ZMP is within the support region but verges on losing balance as it nears the boundary.

The ZMP-based balance criterion can be directly applied for trajectory planning or control, usually in fully actuated systems for walking bipedal robots and other kinds of walking robots (Al-Shuka et al. 2016). Aphiratsakun and Parnichkun (2009) generate a trajectory satisfying the ZMP balance criterion and use the error between desired ZMP and measured CoP as an input to a feedback fuzzy logic controller for balance control on their 12 degree-of-freedom (DoF) lower-limb exoskeleton. Ugurlu et al. (2016) modulate ankle stiffness for balance using a derived relation between ankle stiffness and ZMP on their 6 DoF lower-limb exoskeleton. See (Al-Shuka et al. 2016) for a review on various balance strategies in bipedal robots.

However, direct application of ZMP in control may be difficult or impossible due to lacking full actuation of the system, or requiring measurement of ground reaction forces or accurate estimation of joint accelerations. Alternatively, the ZMP-based balance criterion can be used for offline analysis on the viability for balance of a given control strategy discussed in the literature. The cart-pendulum system is a hallmark of balance control strategy investigation in an underactuated 2 DoF system, which has been investigated in Wang et al. (1996) with a fuzzy logic controller and Irfan et al. (2018) with various sliding mode controllers, for instance. Similarly, acrobot is a double pendulum with actuation only at the second joint and is another common underactuated 2 DoF system. This system been used for balance strategy investigation in sources such as in Brown and Passino (1997) where the authors compare PD control with partial feedback linearization, linear-quadratic regulator, and fuzzy logic control. Azad and Featherstone (2016) use a planar 3 DoF triple pendulum in simulation for investigation of a momentum-based control strategy for crouch-to-stand motion. Scalera et al. (2020) applied a PD plus feedforward with partial feedback linearization position control strategy on their underactuated 3 DoF extendable single-link cable-driven pendulum with orientable end effector. The authors use adaptive oscillators for real-time estimation of pendulum phase for trajectory planning. Similar feedback linearization-based approaches or adaptive oscillator-based trajectory generation may be applied in balance applications for control and path planning. Ansari and Murphey (2016) demonstrated a model predictive control-based strategy on various underactuated systems including a cart-pendulum system, double pendulum with actuation at the base joint (pendubot) or second joint (acrobot), and spring-loaded inverted pendulum.

This paper builds upon the work of Azad and Featherstone (2016) by describing a similarly defined controller based on angular momentum but developed for an underactuated triple pendulum rather than double pendulum. This work also experimentally verifies the control strategy using a prototype powered pediatric lower-limb orthosis frame, attached to a test dummy. First, the dynamics of the legs of the orthosis-dummy system are mathematically modeled and experimentally identified. Second, the momentum-based controller is described as it is applied to a triple pendulum system. The control synthesis procedure is described as a closed-loop pole placement problem using the linearized closed-loop system. Third, the momentum-based controller is synthesized using the identified model and is applied in simulation for numerous initial conditions to determine the region of viability not resulting in hyperextension of the knee or loss of balance using a ZMP analysis. A similarly-synthesized linear-quadratic regulator is also used for comparison purposes. Fourth, both controllers are applied experimentally to move the system from a crouched position to an upright, balanced configuration.

A clear next step from the work of Azad and Featherstone (2016) is to apply a control strategy similar to their momentum-based controller, which was based a double pendulum, to other systems. The first main contribution of this work takes this step by extending their work through the development a momentum-based controller for a triple pendulum system in a straightforward manner. Second, this work expands on the limitations of the control strategy presented by Azad and Featherstone through controller comparisons in not only simulations but also experiments, at least for the triple pendulum formulation in this paper. The work of Azad and Featherstone only consider idealized differences from the nominal system in simulation whereas this paper considers an imperfect system through experimental implementation in hardware and determines the feasibility of the control strategy in an orthotic device. Third, this paper reports the first control experiments in the prototype pediatric orthosis with potential for assisting subjects with standing balance or crouch-to-stand motion. This paper, along with some of the authors' prior work (Laubscher et al. 2017; Laubscher and Sawicki 2019a), lays a foundation that is necessary prior to achieving the long-term goal for the pediatric orthosis of eventual subject testing with children with cerebral palsy.

2 Hardware description and system dynamics

A powered pediatric lower-limb orthosis is used as a testing platform for crouch-to-stand control in this paper. The orthosis was developed for assistance and rehabilitation of children from 6 to 11 years of age with walking impairment from gait disorders such as cerebral palsy. The device drives the hip and knee joints using 70 W brushless DC motors via a 3-stage toothed-belt transmission with a speed-reduction ratio

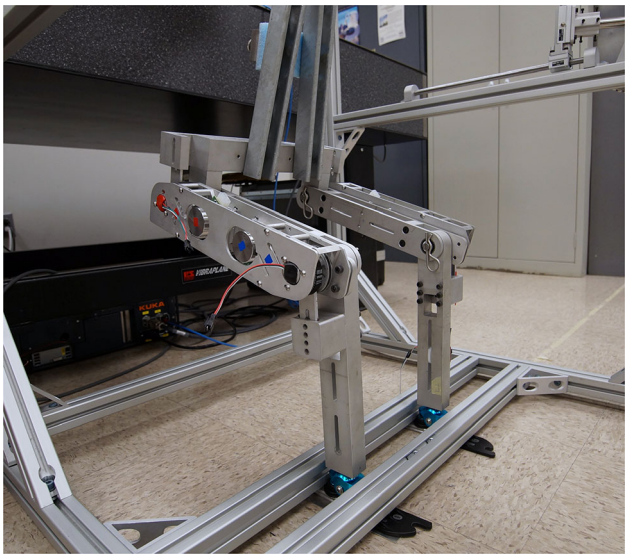

Fig. 1 Orthosis mounted on the dummy

Table 1 Body segment link lengths

Link	Segment	Length L_k (m)
1	Shank	0.300
2	Thigh	0.301
3	Trunk	0.472

of 40.6:1 using identical actuators at both joints. The ankle joint is unactuated. The design requirements and experimental evaluation of the actuators can be found in the authors' earlier work (Laubscher et al. 2017). The actuator capabilities were experimentally tested when driven by a voltage source of 48 V, the nominal voltage rating of the motors. The actuators can provide approximately 17.2 Nm of short-duration torque, maintain approximately 4.2 Nm of continuous torque, and operate at speeds up to 480 deg/s. The hip and knee joint angles are directly measured via magnetic angle sensors in the actuators, and velocities are measured using Hall-effect sensors in the motor and scaled by the transmission ratio. The ankle angle and velocity are inferred from the orientation and movement of the shank as measured by an inertial measurement unit (IMU) using sensor fusion of the gyroscope and accelerometer measurements via a manually-tuned complementary filter (Gui et al. 2015).

The momentum-based control law described in this paper is experimentally evaluated on a prototype powered pediatric lower-limb orthosis frame attached to a test dummy, which is depicted in Fig. 1. The dummy allows free motion at the hip and knee joints and relies on bilateral ankle–foot prostheses for passive stiffness and damping at the ankle joints. The components are sized for the body segment lengths of an average 8 year old child (Fryar et al. 2012; Winter 2009), with link lengths tabulated in Table 1.

In the proceeding subsections, the equation of motion is described for the legs of the system, a ZMP analysis is discussed, and the system model is identified. For the purpose of identification of the complete orthosis-dummy system, the triple pendulum model is identified separately from the ankle stiffness model since linear regression techniques are directly applicable to robotic systems such as pendulums but are not suitable for the ankle model identification. However, direct identification of the triple pendulum proved difficult in practice, so the shank model is identified separately from the thigh-torso model, which are combined to form the complete triple pendulum model.

2.1 Equation of motion

Each leg of the orthosis-dummy system is represented as two independent but identical triple pendulums, depicted in Fig. 2, when the foot is in complete contact with the ground and bilateral interaction at the hip and shared torso is neglected. The nominal dynamics of the system are

$$\boldsymbol{u} = \boldsymbol{Y}_{\mathrm{n}}\boldsymbol{\Phi}_{\mathrm{n}} = \begin{bmatrix} gc_1 & \dot{\omega}_1 & Y_{13} & \dot{\omega}_2 & Y_{15} & \dot{\omega}_3 \\ 0 & 0 & Y_{23} & \dot{\omega}_2 & Y_{25} & \dot{\omega}_3 \\ 0 & 0 & 0 & 0 & Y_{35} & \dot{\omega}_3 \end{bmatrix} \boldsymbol{\Phi}_{\mathrm{n}} \tag{1}$$

where

$$\begin{aligned} Y_{13} &= -L_1 s_2 \dot{q}_2^2 + gc_{12} + 2L_1 \ddot{q}_1 c_2 + L_1 \ddot{q}_2 c_2 - 2L_1 s_2 \dot{q}_1 \dot{q}_2 \\ Y_{23} &= L_1 s_2 \dot{q}_1^2 + gc_{12} + L_1 c_2 \ddot{q}_1 \\ Y_{35} &= s_3\big(c_2\big(L_1 \dot{q}_1^2 - gs_1\big) - s_2(L_1 \ddot{q}_1 + gc_1) + L_2(\dot{q}_1 + \dot{q}_2)^2\big) \\ &\quad + c_3\big(c_2(L_1 \ddot{q}_1 + gc_1) + s_2\big(L_1 \dot{q}_1^2 - gs_1\big) + L_2(\ddot{q}_1 + \ddot{q}_2)\big) \\ Y_{25} &= Y_{35} + L_2 c_3 \dot{\omega}_3 - L_2 s_3 \omega_3^2 \\ Y_{15} &= Y_{25} + L_1 c_{23} \dot{\omega}_3 - L_1 s_{23} \omega_3^2 \end{aligned}$$

$$\begin{aligned} c_j &= \cos\big(q_j\big), \quad c_{jk} = \cos\big(q_j + q_k\big), \quad c_{123} = \cos(q_1 + q_2 + q_3) \\ s_j &= \sin\big(q_j\big), \quad s_{jk} = \sin\big(q_j + q_k\big), \quad s_{123} = \sin(q_1 + q_2 + q_3) \end{aligned}$$

$$\omega_k = \sum_{j=1}^{k} \dot{q}_j \qquad \dot{\omega}_k = \sum_{j=1}^{k} \ddot{q}_j \qquad \boldsymbol{\Phi}_{\mathrm{n}} = \begin{bmatrix} m_1 x_1 + (m_2 + m_3) L_1 \\ I_1 + m_1 x_1^2 + (m_2 + m_3) L_1^2 \\ m_2 x_2 + m_3 L_2 \\ I_2 + m_2 x_2^2 + m_3 L_2^2 \\ m_3 x_3 \\ I_3 + m_3 x_3^2 \end{bmatrix}$$

and the unknown inertial parameters are described in Table 2.

2.2 Zero-moment point

In bipedal robots, balance is ensured when the ground-contact components are able to provide the necessary forces

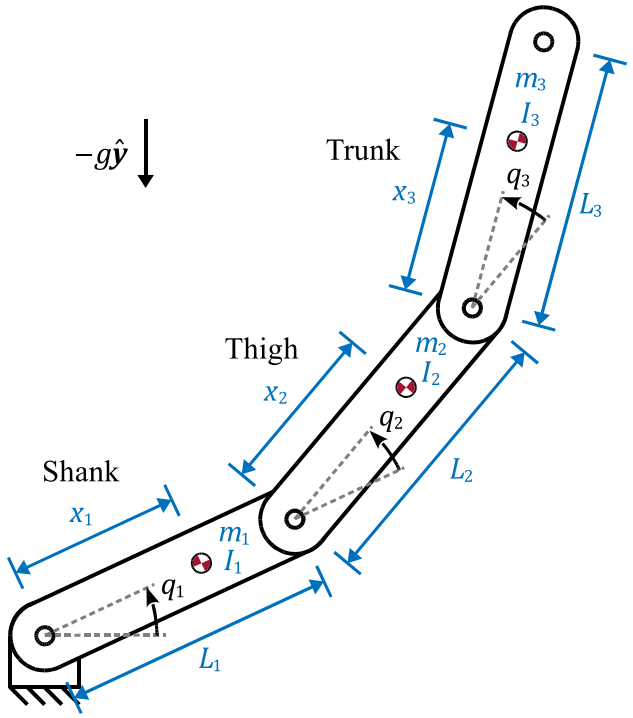

Fig. 2 Schematic of the triple pendulum representing a leg of the orthosis-dummy system

Table 2 Nomenclature for link parameters

Variable	Description
m_k	Mass of link k
x_k	Center of mass (CoM) of link k from joint k
I_k	Moment of inertia of link k at its COM

and moments required to prevent the system CoP from leaving the base of support. In the orthosis-dummy system in this work, the ground-contact components are the bottom of the ankle–foot prostheses. One condition often used to check if the system is balanced is to test if the ZMP is within the support region of the system (Siciliano and Khatib 2008; Vukobratović and Borovac 2004). If this computed point is outside this region, the system is not balanced.

By definition, the ZMP $\boldsymbol{p}$ is a point such that the equivalent reaction moment has zero horizontal components. In effect, the net reaction force $\boldsymbol{f}$ can be relocated to the point $\boldsymbol{p}$ so that the resulting net reaction torque $\boldsymbol{\tau}$ remains equal

$$\boldsymbol{\tau} = \boldsymbol{p} \times \boldsymbol{f} + R\boldsymbol{n} \tag{2}$$

where R is the signed magnitude of the reaction moment in the vertical direction $\boldsymbol{n}$, which is the unit vector normal to the surface of the ground. From the definition, the ZMP lies on the ground so $\boldsymbol{p} \cdot \boldsymbol{n} = p_g$, where p_g is the signed distance from the origin to the ground in the direction $\boldsymbol{n}$. There are three equations represented by (2) with three unknowns: the scalar R and two dimensions of the vector $\boldsymbol{p}$. By taking the dot product of both sides by $\boldsymbol{f}$, R can be solved.

$$\boldsymbol{\tau} \cdot \boldsymbol{f} = (\boldsymbol{p} \times \boldsymbol{f}) \cdot \boldsymbol{f} + R(\boldsymbol{n} \cdot \boldsymbol{f}) \quad \Rightarrow \quad R = \frac{\boldsymbol{\tau} \cdot \boldsymbol{f}}{\boldsymbol{n} \cdot \boldsymbol{f}} \tag{3}$$

Also, by taking the dot product of both sides of (2) by $\boldsymbol{p}$, a useful expression can be found.

$$\boldsymbol{\tau} \cdot \boldsymbol{p} = (\boldsymbol{p} \times \boldsymbol{f}) \cdot \boldsymbol{p} + R(\boldsymbol{n} \cdot \boldsymbol{p}) = \frac{\boldsymbol{\tau} \cdot \boldsymbol{f}}{\boldsymbol{n} \cdot \boldsymbol{f}} p_g \tag{4}$$

By taking the cross product of both sides of (2) by $\boldsymbol{\tau}$, taking advantage of the vector triple product property, and substituting in (3) and (4), $\boldsymbol{p}$ can be solved.

$$\begin{aligned}
\boldsymbol{\tau} \times \boldsymbol{\tau} &= \boldsymbol{\tau} \times (\boldsymbol{p} \times \boldsymbol{f}) + R(\boldsymbol{\tau} \times \boldsymbol{n}) \\
\boldsymbol{0} &= (\boldsymbol{\tau} \cdot \boldsymbol{f})\boldsymbol{p} - (\boldsymbol{\tau} \cdot \boldsymbol{p})\boldsymbol{f} + R(\boldsymbol{\tau} \times \boldsymbol{n}) \\
(\boldsymbol{\tau} \cdot \boldsymbol{f})\boldsymbol{p} &= \frac{\boldsymbol{\tau} \cdot \boldsymbol{f}}{\boldsymbol{n} \cdot \boldsymbol{f}} p_g \boldsymbol{f} - \frac{\boldsymbol{\tau} \cdot \boldsymbol{f}}{\boldsymbol{n} \cdot \boldsymbol{f}} (\boldsymbol{\tau} \times \boldsymbol{n}) \\
\boldsymbol{p} &= \frac{p_g \boldsymbol{f} + \boldsymbol{n} \times \boldsymbol{\tau}}{\boldsymbol{n} \cdot \boldsymbol{f}}
\end{aligned} \tag{5}$$

This general formulation for the ZMP agrees with the formula given in Siciliano and Khatib (2008) for the special case when $\boldsymbol{n} = \hat{z}$.

This equation shows that if the net reaction force and torque vectors are measured, the ZMP can be directly calculated. Alternatively, the net reaction force and torque vectors can be computed using a model of the system and application of Newton–Euler's laws of motion for rigid body dynamics: $\boldsymbol{f} = \dot{\boldsymbol{P}} - m\boldsymbol{g}$ and $\boldsymbol{\tau} = \dot{\boldsymbol{L}} - \boldsymbol{C} \times (m\boldsymbol{g})$ where the entire system's linear momentum is $\boldsymbol{P}$, angular momentum is $\boldsymbol{L}$, mass is m, and center of mass (CoM) vector is $\boldsymbol{C}$. Using these two relations, this gives the *computed* ZMP and is calculated based on the motion of the system.

For an N-link system, the time derivative of the linear momentum vector can be calculated by differentiating the sum of the constituent parts from each link.

$$\boldsymbol{P} = \sum_{i=1}^{N} m_i \dot{\boldsymbol{C}}_i \qquad \dot{\boldsymbol{P}} = \sum_{i=1}^{N} m_i \ddot{\boldsymbol{C}}_i \tag{6}$$

Similarly, the angular momentum vector can be calculated from its constituent parts, and its time derivative can be found using differentiation and using the special property relating $\dot{\boldsymbol{R}}$ with the skew-symmetric cross-product matrix of $\boldsymbol{\omega}$ and the rotation matrix $\boldsymbol{R}$ itself (Spong et al. 2006).

$$\boldsymbol{L} = \sum_{i=1}^{N} \left(\boldsymbol{C}_i \times \left(m_i \dot{\boldsymbol{C}}_i \right) + \boldsymbol{R}_i \boldsymbol{I}_i \boldsymbol{R}_i^{\mathrm{T}} \boldsymbol{\omega}_i \right)$$

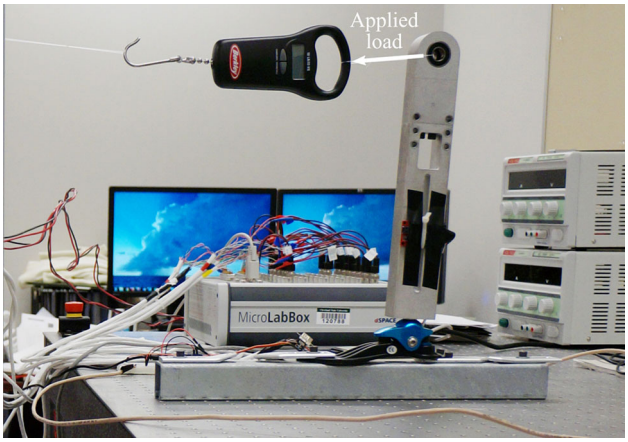

Fig. 3 Experimental setup for determining the ankle stiffness model and shank model

$$\dot{\boldsymbol{L}} = \sum_{i=1}^{N} \left(\boldsymbol{C}_i \times \left(m_i \ddot{\boldsymbol{C}}_i \right) + \boldsymbol{\omega}_i \times \left(\boldsymbol{R}_i \boldsymbol{I}_i \boldsymbol{R}_i^{\mathrm{T}} \boldsymbol{\omega}_i \right) + \boldsymbol{R}_i \boldsymbol{I}_i \boldsymbol{R}_i^{\mathrm{T}} \dot{\boldsymbol{\omega}}_i \right) \tag{7}$$

In summary, the joint positions, velocities, and accelerations can be used to calculate the kinematics of the system, including the rotation matrices, motion of the centers of mass, and link angular velocities and accelerations. These can then be used to compute the time derivative of the linear momentum $\dot{\boldsymbol{P}}$ using (6) and angular momentum $\dot{\boldsymbol{L}}$ using (7), which in turn can be used to calculate the computed ZMP $\boldsymbol{p}$ using (5).

2.3 Ankle stiffness model

The Truper prostheses (College Park Industries, Michigan, USA) used for the ankle dynamics in the dummy exhibits stiffness behavior where the moment-displacement relationship is not explicitly quantified by the manufacturer. To identify the ankle stiffness model, the foot-shank system was mounted on a tabletop and a measured load was applied horizontally to the system, depicted in Fig. 3, which resulted in a known moment at the ankle. The load was incrementally increased, gradually displacing the ankle as measured by the shank-mounted IMU. For each applied known load, a displacement was measured after the system settled. This process was applied for both the dorsiflexion and plantarflexion directions. The resulting load–displacement curve is shown in Fig. 4.

The load–displacement curve exhibited larger stiffness in the dorsiflexion direction than in the plantarflexion direction, with a nonlinear transition near the neutral position. A model was chosen as a weighted sum of two linear stiffness terms

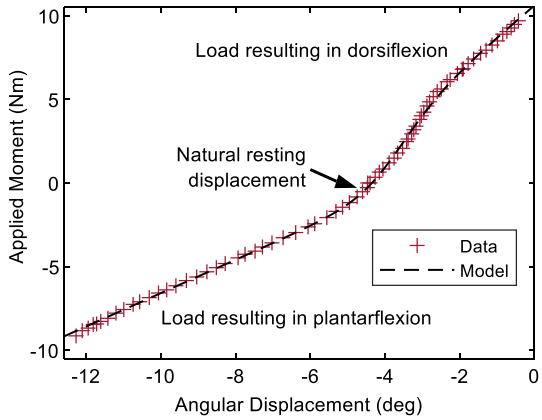

Fig. 4 Applied ankle moment versus resultant angular displacement in the experiment to determine the ankle stiffness model

Table 3 Ankle stiffness model parameters

Parameter	Value
k_{p}	57.1 Nm/rad
k_{d}	109 Nm/rad
θ_{p}	− 0.0593 rad
θ_{d}	− 0.0978 rad
θ_0	− 0.0665 rad
β	0.0103 rad

where the weights were written in terms of a sigmoid function for a smooth transition

$$\begin{aligned} M_{\mathrm{a}}(\theta) = &\left(1 - S_\beta(\theta - \theta_0)\right) k_{\mathrm{p}}(\theta - \theta_{\mathrm{d}}) \\ &+ S_\beta(\theta - \theta_0) k_{\mathrm{d}}(\theta - \theta_{\mathrm{d}}) \end{aligned} \tag{8}$$

where

$$S_\beta(\theta) = \frac{1}{1 - e^{-\theta/\beta}}.$$

The parameters in the ankle stiffness model (8) were determined using a quasi-Newton nonlinear numerical optimization solver. The resulting parameters are tabulated in Table 3 with the ankle moment predicted by the model also included in Fig. 4. The root-mean-square (RMS) moment prediction error is 0.13 Nm.

2.4 Shank model

The shank identification experiment used a similar set up to the ankle stiffness model identification experiment in Fig. 3. Step response data were collected by applying a horizontal load to the system via cable to set the initial position of the ankle and then instantaneously releasing the load by cutting the cable. This process was applied for an initial position both in the dorsiflexion and plantarflexion directions and resulting response data were collected using the shank-mounted IMU.

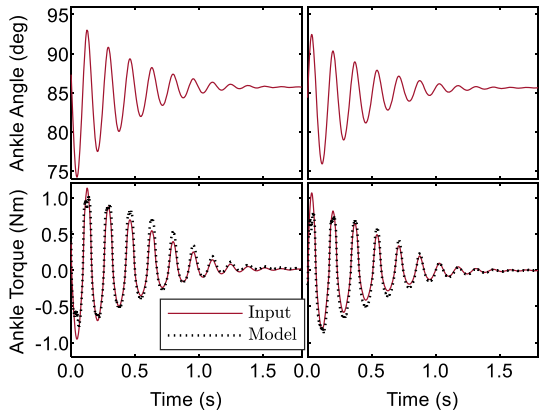

Fig. 5 Applied ankle moment versus resultant angular displacement in the experiment to determine the ankle stiffness model

A brief portion of collected data right after the release of the load was removed to avoid the undesired but unavoidable interaction from the experimenter when performing the cut of the cable. The system responses are shown in Fig. 5.

The shank system was modeled as a single pendulum system augmented with viscous friction terms differing in value based on whether the ankle was in plantarflexion or dorsiflexion

$$\begin{aligned} u_1 &= \boldsymbol{Y}_{\text{sn}}\boldsymbol{\Phi}_{\text{sn}} + \boldsymbol{Y}_{\text{sa}}\boldsymbol{\Phi}_{\text{sa}} \\ &= \left[\, g c_1 \;\; \ddot{q}_1 \,\right]\boldsymbol{\Phi}_{\text{sn}} + \left[\, \langle q_1 < q_{\text{r}}\rangle \dot{q}_1 \;\; \langle q_1 > q_{\text{r}}\rangle \dot{q}_1 \,\right]\boldsymbol{\Phi}_{\text{sa}} \end{aligned} \tag{9}$$

where

$$\begin{aligned} \boldsymbol{\Phi}_{\text{sn}} &= \left[\, m_1 x_1 \;\; I_1 + m_1 x_1^2 \,\right]^{\text{T}} \\ \boldsymbol{\Phi}_{\text{sa}} &= \left[\, d_{\text{ap}} \;\; d_{\text{ad}} \,\right]^{\text{T}} \\ \langle P \rangle &= \begin{cases} 1 \text{ if } P \text{ is true} \\ 0 \text{ if } P \text{ is false} \end{cases}. \end{aligned}$$

Smoothing splines were fit to the measured position data using a smoothing parameter of $1\text{–}10^{-8}$ which was then differentiated once and twice to obtain the angular velocity and acceleration, respectively. The threshold between dorsiflexion and plantarflexion q_{r} was found manually. These data were substituted into (9) using the ankle stiffness model (8) as the input. The unknown parameters were found using linear regression and are provided in Table 4. The moment predicted by the model is included in Fig. 5 and has an RMS moment prediction error of 0.042 Nm for both step response experiments combined.

2.5 Thigh-torso model

The thigh and torso were identified together using single double pendulum model. This was chosen in opposition to two separate thigh and torso models since many terms in the double pendulum model directly match terms in the triple pendulum model and to avoid the accumulation of errors prone in each identification process. The assembled system was affixed upside down such that the shank was rigidly attached to a grounded testing platform, depicted in Fig. 6. In this scenario, the thigh-torso system was fully actuated so articulation of each DoF was possible. An open-loop identification approach was taken by applying an excitation torque to each joint. The excitation signal was designed such that the knee and hip joint torques were sinusoidal with 11 and 10 cycles, respectively, over 30 s. This generated a torque curve with two sine waves with frequencies of 0.367 and 0.333 Hz that start out of phase and transition into and back out of phase. Four periods were combined for a total of 120 s of data. The amplitudes were chosen as 6.0 and 2.5 Nm for the knee and hip joints, respectively. The supplied torque and joint angle response are depicted in Fig. 7.

The thigh-torso system was modeled as a double pendulum system augmented with viscous friction, Coulomb friction, and torque measurement bias

$$\begin{aligned} \begin{bmatrix} u_2 \\ u_3 \end{bmatrix} &= \boldsymbol{Y}_{\text{ttn}}\boldsymbol{\Phi}_{\text{ttn}} + \boldsymbol{Y}_{\text{tta}}\boldsymbol{\Phi}_{\text{tta}} \\ &= \begin{bmatrix} g c_1 & \dot{\omega}_1 & Y_{\text{tt13}} & \dot{\omega}_2 \\ 0 & 0 & Y_{\text{tt23}} & \dot{\omega}_2 \end{bmatrix}\boldsymbol{\Phi}_{\text{ttn}} \end{aligned}$$

Table 4 Shank model parameters

Parameter	Value
$m_1 x_1$	0.00415 kg m
$I_1 + m_1 x_1^2$	0.00452 kg m^2
d_{ap}	0.0176 Nm s/rad
d_{ad}	0.0266 Nm s/rad

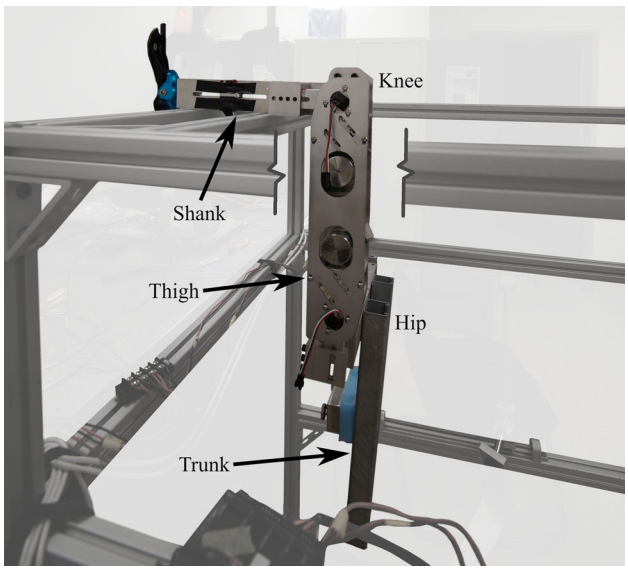

Fig. 6 Experimental setup for the identification of the thigh-torso double pendulum model

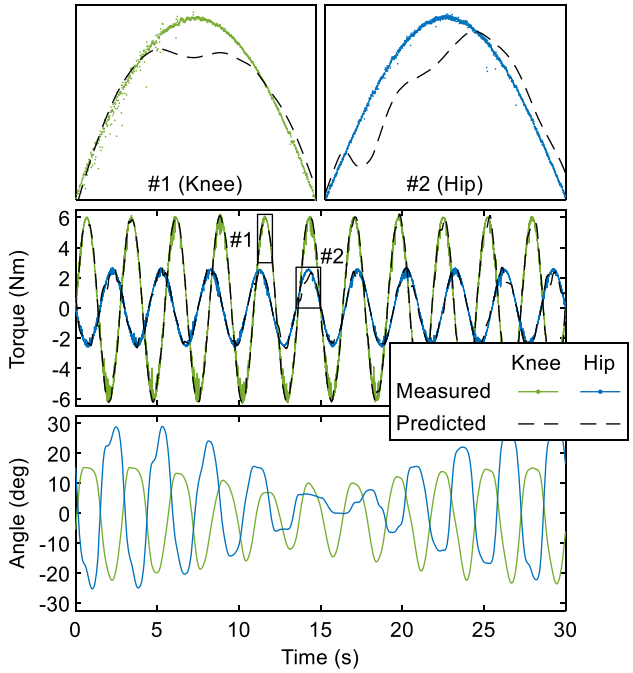

Fig. 7 Experimental results for identification of the thigh-torso double pendulum model

$$+\begin{bmatrix} \dot{q}_1 & 0 & \mathrm{sgn}(\dot{q}_1) & 0 & 1 & 0 \\ 0 & \dot{q}_2 & 0 & \mathrm{sgn}(\dot{q}_2) & 0 & 1 \end{bmatrix} \boldsymbol{\Phi}_{\mathrm{tta}} \tag{10}$$

where $\mathrm{sgn}(\dot{q}_k)$ is the sign function, approximated as $2S_{0.05}(\dot{q}_k) - 1$ for the purpose of identification, and

$$Y_{\mathrm{tt23}} = c_2(L_2\ddot{q}_1 + gc_1) + s_2\left(L_2\dot{q}_1^2 - gs_1\right)$$
$$Y_{\mathrm{tt13}} = Y_{\mathrm{tt23}} - L_2 s_2(\dot{q}_1 + \dot{q}_2)^2 + L_2 c_2(\ddot{q}_1 + \ddot{q}_2)$$
$$\boldsymbol{\Phi}_{\mathrm{ttn}} = \begin{bmatrix} m_2x_2 + m_3L_2 & I_2 + m_2x_2^2 + m_3L_2^2 & m_3x_3 & I_3 + m_3x_3^2 \end{bmatrix}^{\mathrm{T}}$$
$$\boldsymbol{\Phi}_{\mathrm{tta}} = \begin{bmatrix} d_{\mathrm{k}} & d_{\mathrm{h}} & c_{\mathrm{k}} & c_{\mathrm{h}} & b_{\mathrm{k}} & b_{\mathrm{h}} \end{bmatrix}^{\mathrm{T}}.$$

The thigh-torso model was identified using the same technique used identify the shank model. A smoothing spline with a smoothing parameter of 0.99 was fit to the measured position data and was differentiated once and twice to calculate joint velocities and accelerations, respectively. These data were substituted into (10) where the input was the applied torque to the system. Linear regression was applied, and the resulting unknown inertial parameters are tabulated in Table 5. The torque predicted from the model is included in Fig. 7 and has an RMS error of 0.291 Nm and 0.262 Nm for the knee and hip joints, respectively.

2.6 Complete orthosis model

The identified shank model and the thigh-torso model can be combined to form the triple pendulum model. By observing the similarities in the nominal parameters in the triple pendulum model (1) to the parameters in the shank model (9) and thigh-torso model (10), a relation can be found.

Table 5 Thigh-torso model parameters

Parameter	Value
$m_2x_2 + m_3L_2$	2.5714 kg m
$I_2 + m_2x_2^2 + m_3L_2^2$	0.7428 kg m^2
m_3x_3	1.1799 kg m
$I_3 + m_3x_3^2$	0.3299 kg m^2
d_{k}	0.2652 Nm s/rad
d_{h}	0.2228 Nm s/rad
c_{k}	0.6882 Nm
c_{h}	0.6038 Nm
b_{k}	0.1615 Nm
b_{h}	− 0.3126 Nm

$$\boldsymbol{\Phi}_{\mathrm{n}} = \begin{bmatrix} m_1x_1 + (m_2+m_3)L_1 \\ I_1 + m_1x_1^2 + (m_2+m_3)L_1^2 \\ m_2x_2 + m_3L_2 \\ I_2 + m_2x_2^2 + m_3L_2^2 \\ m_3x_3 \\ I_3 + m_3x_3^2 \end{bmatrix} = \begin{bmatrix} \boldsymbol{\Phi}_{\mathrm{sn}} \\ \hline \boldsymbol{\Phi}_{\mathrm{ttn}} \end{bmatrix} + \begin{bmatrix} (m_2+m_3)L_1 \\ (m_2+m_3)L_1^2 \\ \hline \mathbf{0}_{4\times 1} \end{bmatrix} \tag{11}$$

The additional term can be calculated from the measured total thigh-torso mass $m_2 + m_3 = 9.47$ kg and known shank length $L_1 = 0.300$ m. The complete model, including non-nominal terms, then becomes

$$\boldsymbol{u} = \left[\begin{array}{c|cc} \boldsymbol{Y}_{\mathrm{n}} & \boldsymbol{Y}_{\mathrm{sa}} & \mathbf{0} \\ & \mathbf{0}_{2\times 1} & \boldsymbol{Y}_{\mathrm{tta}} \end{array}\right] \begin{bmatrix} \boldsymbol{\Phi}_{\mathrm{n}} \\ \hline \boldsymbol{\Phi}_{\mathrm{sa}} \\ \boldsymbol{\Phi}_{\mathrm{tta}} \end{bmatrix} \tag{12}$$

where the complete set of inertial parameters are given in Table 6.

3 Momentum-based controller

The control law described in this section is based on the work of Azad and Featherstone (2016) where the authors describe a controller for crouch-to-stand motion of an underactuated double pendulum system in simulation. This section extends their work by modifying the concepts they introduced to an underactuated triple pendulum where the first joint is unactuated, and the other joints are actuated.

For static balance, the CoM of the system should be driven to directly above the ankle joint with no velocity. As dis-

Table 6 Triple pendulum model parameters

Parameter	Value
$\Phi_1 = m_1 x_1 + (m_2 + m_3) L_1$	2.8450 kg m
$\Phi_2 = I_1 + m_1 x_1^2 + (m_2 + m_3) L_1^2$	0.8568 kg m^2
$\Phi_3 = m_2 x_2 + m_3 L_2$	2.5714 kg m
$\Phi_4 = I_2 + m_2 x_2^2 + m_3 L_2^2$	0.7428 kg m^2
$\Phi_5 = m_3 x_3$	1.1799 kg m
$\Phi_6 = I_3 + m_3 x_3^2$	0.3299 kg m^2
$\Phi_7 = d_{\mathrm{ap}}$	0.0176 Nm s/rad
$\Phi_8 = d_{\mathrm{ad}}$	0.0266 Nm s/rad
$\Phi_9 = d_{\mathrm{k}}$	0.2652 Nm s/rad
$\Phi_{10} = d_{\mathrm{h}}$	0.2228 Nm s/rad
$\Phi_{11} = c_{\mathrm{k}}$	0.6882 Nm
$\Phi_{12} = c_{\mathrm{h}}$	0.6038 Nm
$\Phi_{13} = b_{\mathrm{k}}$	0.1615 Nm
$\Phi_{14} = b_{\mathrm{h}}$	− 0.3126 Nm

cussed in the work of Azad and Featherstone (2016) for the double pendulum, an equivalent condition for static balance is for angular momentum and its first and second derivatives to be equal to zero $L = \dot{L} = \ddot{L} = 0$. When these conditions are met, the CoM vector of the system relative the ankle joint $\boldsymbol{C}$ has zero horizontal component C and the joint velocities $\dot{\boldsymbol{q}}$ are equal to zero. A similar relation holds for the triple pendulum. This is because $\dot{L} = 0$ if and only if $C = 0$ due to Euler's law of motion, and $L = \ddot{L} = 0$ is satisfied when $\dot{\boldsymbol{q}} = \boldsymbol{0}$ since L and $\ddot{L}$ are both linear in $\dot{\boldsymbol{q}}$. Unlike in the double pendulum case, the converse of the velocity relation does not generally hold for the triple pendulum. The conditions for joint velocities when $L = \ddot{L} = 0$ holds is detailed in "Appendix 1".

The net angular momentum of the system along the ankle joint axis follows from taking the sum of the constituent angular momenta of the links from translational and rotational motion, which can be represented in a form linear in the inertial parameters. For the planar triple pendulum system, the z-component of (7) becomes

$$\begin{aligned} L &= \sum_{k=1}^{3} m_k \left(\boldsymbol{C}_k \times \dot{\boldsymbol{C}}_k\right) \cdot \hat{\boldsymbol{z}} + I_k \omega_k = \boldsymbol{L} \boldsymbol{\Phi}_{\mathrm{n}} \\ &= \begin{bmatrix} 0 \\ \omega_1 \\ L_1(\omega_1 + \omega_2) c_2 \\ \omega_2 \\ L_1(\omega_1 + \omega_3) c_{23} + L_2(\omega_2 + \omega_3) c_3 \\ \omega_3 \end{bmatrix}^{\mathrm{T}} \boldsymbol{\Phi}_{\mathrm{n}}. \end{aligned} \tag{13}$$

Euler's second law of motion from rigid body dynamics states that that the time derivative of this angular momentum is equal to the net external moment acting on the system. For a nominal triple pendulum system, this is moment results from gravitational effects. The second time-derivative follows from simple differentiation.

$$\begin{aligned} \dot{L} &= -g \sum_{k=1}^{3} m_k \boldsymbol{C}_k \cdot \hat{\boldsymbol{x}} \\ &= \boldsymbol{L}' \boldsymbol{\Phi}_{\mathrm{n}} = \begin{bmatrix} -c_1 g & 0 & -c_{12} g & 0 & -c_{123} g & 0 \end{bmatrix} \boldsymbol{\Phi}_{\mathrm{n}} \\ \ddot{L} &= \boldsymbol{L}'' \boldsymbol{\Phi}_{\mathrm{n}} = \begin{bmatrix} \omega_1 s_1 g & 0 & \omega_2 s_{12} g & 0 & \omega_3 s_{123} g & 0 \end{bmatrix} \boldsymbol{\Phi}_{\mathrm{n}} \end{aligned} \tag{14}$$

Motivated to drive angular momentum and its derivatives to zero and following a similar control scheme from Azad and Featherstone (2016), the momentum-based controller (MBC) developed for the triple pendulum is defined as a linear combination of angular momentum and its derivatives with coefficients $k_{\mathrm{h}j}$ and $k_{\mathrm{k}j}$ for $j \in \{0,1,2\}$ as controller gains.

$$\begin{bmatrix} u_2 \\ u_3 \end{bmatrix} = \begin{bmatrix} k_{\mathrm{h}0} & k_{\mathrm{h}1} & k_{\mathrm{h}2} \\ k_{\mathrm{k}0} & k_{\mathrm{k}1} & k_{\mathrm{k}2} \end{bmatrix} \begin{bmatrix} \boldsymbol{L} \\ \boldsymbol{L}' \\ \boldsymbol{L}'' \end{bmatrix} \boldsymbol{\Phi}_{\mathrm{n}} + \begin{bmatrix} k_{\mathrm{h}} & 0 & 0 \\ 0 & k_{\mathrm{k}} & 0 \end{bmatrix} (\boldsymbol{q} - \boldsymbol{q}_0) + \begin{bmatrix} G_2 \\ G_3 \end{bmatrix} \tag{15}$$

The gravity compensation terms G_2 and G_3 are included to improve performance and a proportional feedback term, with controller gains k_{h} and k_{k}, is included to help drive the system to the equilibrium upright position $\boldsymbol{q}_0 = [\ \pi/2\ 0\ 0\ ]^{\mathrm{T}}$. The controller gains are later selected for stability and adequate performance.

To test if the nonlinearity of the MBC poses any benefit over a simpler, linear memoryless state-feedback controller, the control law (15) is linearized about the operating point $\boldsymbol{q}_0$ with zero velocity. This yields the following control law

$$\begin{aligned} \begin{bmatrix} u_2 \\ u_3 \end{bmatrix} \approx & \begin{bmatrix} 65k_{\mathrm{h}1} + k_{\mathrm{h}} - 37 & 37k_{\mathrm{h}1} - 37 & 12k_{\mathrm{h}1} - 12 \\ 65k_{\mathrm{k}1} - 12 & 37k_{\mathrm{k}1} + k_{\mathrm{k}} - 12 & 12k_{\mathrm{k}1} - 12 \end{bmatrix} (\boldsymbol{q} - \boldsymbol{q}_0) \\ & + \begin{bmatrix} 4.9k_{\mathrm{h}0} + 65k_{\mathrm{h}2} & 2.9k_{\mathrm{h}0} + 37k_{\mathrm{h}2} & 1.0k_{\mathrm{h}0} + 12k_{\mathrm{h}2} \\ 4.9k_{\mathrm{k}0} + 65k_{\mathrm{k}2} & 2.9k_{\mathrm{k}0} + 37k_{\mathrm{k}2} & 1.0k_{\mathrm{k}0} + 12k_{\mathrm{k}2} \end{bmatrix} \dot{\boldsymbol{q}} \end{aligned} \tag{16}$$

which approximates the MBC near the upright configuration for the identified model of the system.

For the orthosis in this paper, the controller used to drive the system $\boldsymbol{K}(\boldsymbol{q}, \dot{\boldsymbol{q}})$ actuates the knee and hip joints (u_2 and u_3, respectively) and is used in conjunction with an ankle—foot prosthesis with passive stiffness $u_1 = M_{\mathrm{a}}(q_1)$. The two sources for inputs to the triple pendulum system $\boldsymbol{G}$ are combined and depicted in Fig. 8 as a block diagram.

3.1 Controller gain selection

The control law gains should be chosen so the system is well-behaved even with the presence of the prosthetic foot.

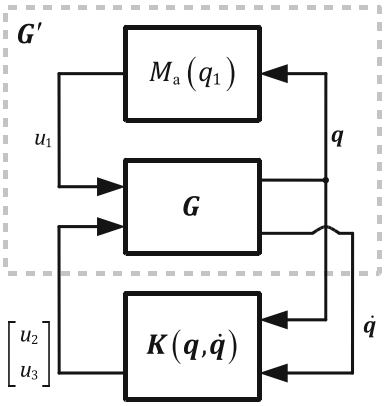

Fig. 8 Block diagram of the triple pendulum plant $\boldsymbol{G}$ with torque inputs from the controller $\boldsymbol{K}(\boldsymbol{q}, \dot{\boldsymbol{q}})$ and ankle–foot prosthesis $M_a(\boldsymbol{q}_1)$

That is, the closed-loop system should be stable, have adequate damping, and respond quickly without requiring too much torque. The closed-loop system, depicted in Fig. 8, is obtained by first substituting the ankle stiffness model (8) into the pendulum model (12) to form the plant $\boldsymbol{G}'$ and then substituting in the controller (15) to form the closed-loop system $\boldsymbol{G}''$. A local analysis is performed by linearizing the closed-loop system about the equilibrium position $\boldsymbol{q}_0$ with zero velocity and calculating the eigenvalues of the system matrix

$$\lambda_k = R_k + I_k i \tag{17}$$

where R_k and I_k is the real and imaginary components, respectively, of eigenvalue λ_k for $k \in \{1,\ldots,6\}$. The system matrix as a function of the controller gains can be found in "Appendix 2".

Numerical optimization is used to solve for the gains in the momentum-based control law based on minimizing the objective function

$$J = w_R \max_{k=1\ldots6} \left| R_k^{-1} \right| + w_I \sum_{k=1}^{6} |I_k| + P. \tag{18}$$

The first term in (18) is used to increase the closed-loop response of the system by locating the real components of the eigenvalues far from the imaginary axis. The second term is used to increase the damping of the closed-loop system and to avert undesired oscillations by bringing the eigenvalues close to the real axis.

The third term in (18) is a penalty term defined as

$$\begin{aligned} P = {} & 10^9 \sum_{k=1}^{6} \langle R_k > 0 \rangle (1 + R_k) \\ & + 10^6 \sum_{j=1}^{2} \sum_{k=1}^{3} \langle P_{jk} > 100 \rangle \left(1 + P_{jk}/100\right) \\ & + 10^6 \sum_{j=1}^{2} \sum_{k=1}^{3} \langle D_{jk} > 10 \rangle \left(1 + D_{jk}/10\right) \end{aligned} \tag{19}$$

where P_{jk} and D_{jk} are the respective elements of

$$\boldsymbol{P} = \left. \frac{\partial \boldsymbol{K}(\boldsymbol{q}, \dot{\boldsymbol{q}})}{\partial \boldsymbol{q}} \right|_{\substack{\boldsymbol{q} = \boldsymbol{q}_0 \\ \dot{\boldsymbol{q}} = \boldsymbol{0}}}, \quad \boldsymbol{D} = \left. \frac{\partial \boldsymbol{K}(\boldsymbol{q}, \dot{\boldsymbol{q}})}{\partial \dot{\boldsymbol{q}}} \right|_{\substack{\boldsymbol{q} = \boldsymbol{q}_0 \\ \dot{\boldsymbol{q}} = \boldsymbol{0}}} \tag{20}$$

and is used to apply constraints in the optimization. The first term in (19) restricts the solution space to controllers which yield locally stable closed-loop systems by keeping the eigenvalues in the left-half plane. The second term restricts the elements of the proportional gain of the linear or linearized controller to 100 Nm/rad. Similarly, the third term restricts the elements of the derivative gain to 10 Nms/rad. This helps prevent the control torques from being too high by contesting the goal of maximizing the system response.

4 Controller design and simulation results

For the purpose of evaluating the controller, the initial conditions were chosen to be in balanced configuration with no velocity. This occurs when the horizontal position of CoM of the system C is directly above the ankle.

$$\begin{aligned} C &= \frac{\begin{bmatrix} c_1 & 0 & c_{12} & 0 & c_{123} & 0 \end{bmatrix} \boldsymbol{\Phi}_n}{m_1 + m_2 + m_3} = 0 \\ &\Rightarrow c_1 \Phi_1 + c_{12} \Phi_3 + c_{123} \Phi_5 = 0 \end{aligned} \tag{21}$$

From this, the ankle q_1, knee angle q_2, or hip angle q_3 can be calculated given the other two joint angles, leaving two algebraic degrees of freedom for the starting configuration. The starting velocity was chosen as zero for the simulations in the subsequent sections.

4.1 Crouch-to-stand response in simulation

The momentum-based control law was synthesized using a simulated annealing optimization program with the objective function discussed in Sect. 3.1 where the control parameters were the decision variables. A set of 100 initial conditions with decision variables bounded from -100 to 100 were randomly generated that satisfy the constraints defined by the penalty in (19). The objective function weights were manually tuned as $w_R = 10$ and $w_I = 1$ and the best performing controller was manually selected from the few controllers with smallest cost values.

$$\begin{bmatrix} k_{h0} & k_{h1} & k_{h2} \\ k_{k0} & k_{k1} & k_{k2} \end{bmatrix} = \begin{bmatrix} -25.8 & -0.38 & 1.9 \\ -13.2 & 0.0 & 1.1 \end{bmatrix}$$

$$k_\mathrm{h} = 2.8 \qquad k_\mathrm{k} = 19.4 \tag{22}$$

The resulting state matrix of the linearized closed-loop system and the associated eigenvalues are included in "Appendix 2".

The MBC approximately behaved as a linear state-feedback control law near the operation point $\boldsymbol{q}_0$ with zero speed. Substituting in the control gains (22) into (16) and rewriting into traditional negative feedback form, this gave the approximate controller

$$\begin{bmatrix} u_2 \\ u_3 \end{bmatrix} \approx -\begin{bmatrix} 58 & 51 & 16 \\ 11 & -8.1 & 11 \end{bmatrix}(\boldsymbol{q} - \boldsymbol{q}_0) - \begin{bmatrix} 5.0 & 6.1 & 5.1 \\ -8.9 & -3.4 & 0.58 \end{bmatrix}\dot{\boldsymbol{q}}. \tag{23}$$

The purpose of this linearized controller is to see if the nonlinearity of the MBC poses any substantial benefit over the simpler, linear controller.

For comparison purposes, a linear-quadratic regulator was also synthesized. The synthesis process was chosen similarly to MBC. The positive definite weight matrices $\boldsymbol{Q}_\mathrm{q}$, $\boldsymbol{Q}_{\dot{\mathrm{q}}}$, and $\boldsymbol{R}$ in the cost function

$$J_\mathrm{LQR} = \int_0^\infty \left(\boldsymbol{q}^\mathrm{T}\boldsymbol{Q}_\mathrm{q}\boldsymbol{q} + \dot{\boldsymbol{q}}^\mathrm{T}\boldsymbol{Q}_{\dot{\mathrm{q}}}\dot{\boldsymbol{q}} + \boldsymbol{u}^\mathrm{T}\boldsymbol{R}\boldsymbol{u}\right) dt \tag{24}$$

were written in terms of the decision variables used in the numerical optimization. The decision variables filled all elements of each of the weights, up to symmetry, giving a total of 24 decision variables. An additional constraint was applied in the numerical optimization problem formulation by adding an additional penalty to restrict the weights to be positive definite. The numerical optimization weights were chosen as the same from MBC as $w_\mathrm{R} = 10$ and $w_\mathrm{I} = 1$, which yielded the linear state-feedback control law

$$\begin{bmatrix} u_2 \\ u_3 \end{bmatrix} = -\begin{bmatrix} 51 & 39 & 20 \\ -20 & -12 & 19 \end{bmatrix}(\boldsymbol{q} - \boldsymbol{q}_0) - \begin{bmatrix} 10 & 8.2 & 4.6 \\ -6.2 & -1.2 & 2.2 \end{bmatrix}\dot{\boldsymbol{q}}. \tag{25}$$

Using the initial balanced configuration $\boldsymbol{q} - \boldsymbol{q}_0 = [\,4 \;\; -23.6 \;\; 54.0\,]^\mathrm{T}$ deg, a simulation was run using each of the control laws. The MBC results are shown and Fig. 9 and the LQR results are shown in Fig. 10, and both include the response in the joint angles, torques, and ZMP. Both controllers were able to successfully bring the system to the upright position when starting in a crouched and balanced configuration. This was accomplished without the ZMP exiting the support region, from − 35 to 110 mm defined by the geometry of the prosthetic feet, and therefore without losing balance.

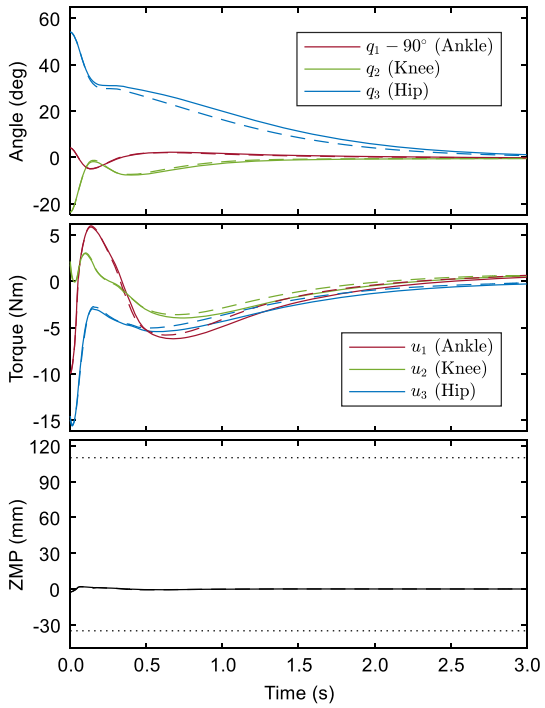

Fig. 9 Simulation of balance control using a momentum-based controller (solid) and its linearization (dashed)

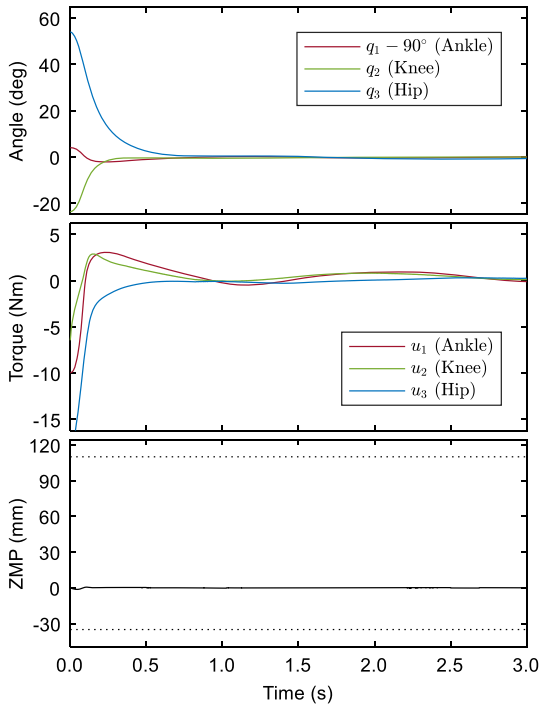

Fig. 10 Simulation of balance control using a linear-quadratic regulator

The LQR more quickly settled the system to within 2 deg of the upright configuration, taking only 0.5 s as compared to the 2.7 s taken by the MBC. However, this was accomplished using a maximum of 21.3 Nm, larger than the 15.5

Nm used by MBC, where both occurred at the hip joint near the initial condition. Unlike with LQR, synthesis of a faster responding MBC proved difficult in the optimization process. This suggests that a fast-responding linear controller can be more easily synthesized using LQR which can outperform MBC, though perhaps at the cost of higher torque usage, at least for the system considered in this work and for the particular initial condition. In addition, the nonlinear MBC performed similar to the linearized MBC, suggesting a linear memoryless state-feedback control law may be adequate choice of control law. The nonlinearity of the control law may add unnecessary complexity to the controller without improving performance. For these reasons, LQR, or more generally a linear memoryless state-feedback control law, may be a better choice of control law as they are capable of performing comparable to or better than the nonlinear MBC. However, these comments must be qualified by how there were many local minima observed in the optimization problem. Most solutions found in the optimization problem gave poor performing controllers, particularly for MBC, and the best performing controllers for both MBC and LQR were hand-picked.

4.2 Region of viability

To evaluate the robustness of the MBC to initial conditions, simulations were run for an array of initial balanced configurations. A simulation was considered a failure when the knee joint hyperextended by at least 2 deg, which is about the average hyperextension permitted in healthy adults (Rubinstein et al. 1995), or the ZMP exited the support region, which was from − 35 to 110 mm for the span of the prosthetic feet. The maximum observed torque in the actuators for each simulation was also quantified.

$$u_{\max} = \max_{i \in \{2,3\},\, t} u_i(t) \tag{26}$$

The set of simulations is used to draw the region of viability to show which initial conditions did not result in a failed simulation by knee hyperextension or loss of balance. The results are shown in Fig. 11 for the MBC and in Fig. 12 for the LQR using the same controllers synthesized from Sect. 4.1. Simulations resulting in hyperextension or loss of balance are marked.

There are a few remarks to be made based on these results. Both controllers were quite robust to the starting initial conditions insofar that neither controller destabilized the system, numerically determined by any joint surpassing 95 deg from the upright configuration at some time throughout the simulation. However, the knee tended to hyperextend for a wide range of initial conditions, at approximately 30 and 44 percent of the considered initial conditions for MBC and LQR,

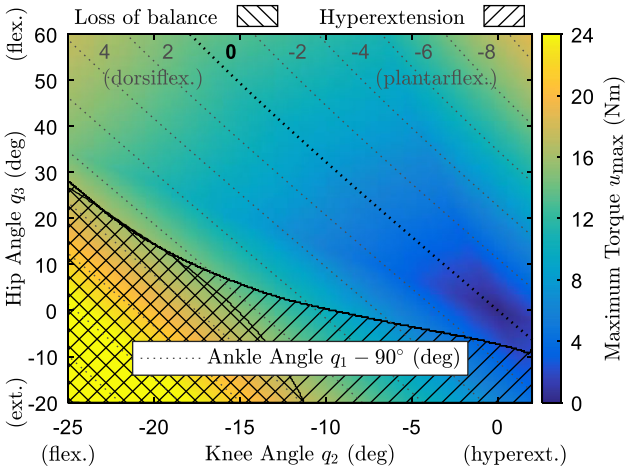

Fig. 11 Region of viability with maximum actuation torque of the orthotic system controlled by a momentum-based controller

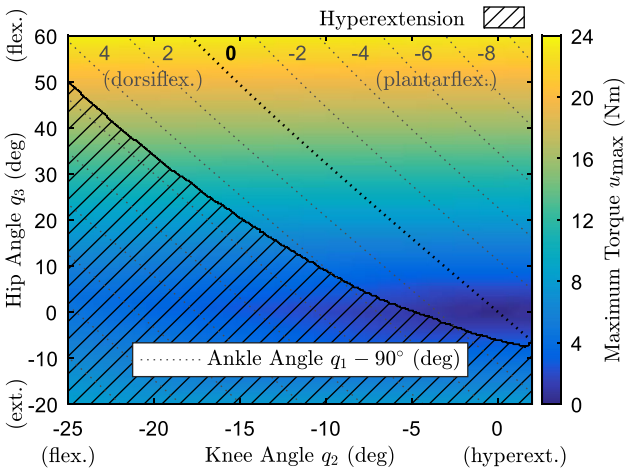

Fig. 12 Region of viability with maximum actuation torque of the orthotic system controlled by a linear-quadratic regulator

respectively. This suggests that MBC may have a better region of viability than LQR, at least for the particular system and controllers considered in this work. This primarily occurred where the knee was initially flexed to any degree and the hip was initially straight or extended (i.e., bottom of plots) or where the knee was initially flexed to a large degree and the hip was extended (i.e., middle to upper left of plots). Though, the threshold for viable initial hip flexion in the MBC was more permissive than the LQR when the knee is initially flexed (i.e., top left of plot). Interestingly, the ZMP balance criterion was satisfied for all simulations using LQR but fails in MBC starting with a flexed knee and straight or extended hip (i.e., bottom left of plots). Though, this region was nearly completely contained in the set of initial conditions that resulted in hyperextension, thereby not decreasing the size of the region of viability by any considerable margin. Other systems considered in the development

of this work (not shown in this paper) did not always show this feature so balance should still be considered in controller development. Within the region of viability, the LQR tended to use larger peak torque than MBC, which is in agreement with observations from Sect. 4.1 when using a particular initial condition. Interestingly, the peak torque in LQR seemed to be primarily a function of the initial hip angle, as opposed to MBC where it was a function of both the initial hip and knee angles. In both LQR and MBC, the peak torque values were reasonable relative to the actuator capability described above in Sect. 2, at approximately 19 Nm and 23 Nm for MBC and LQR, respectively. The actuators should be able to handle the expected torque levels for the considered initial conditions.

5 Experimental results for crouch-to-stand

For experimental validation of the control law, the MBC and LQR were applied to the physical orthotic prototype system described earlier from Sect. 2. However, not all DoF were able to be directly measured as only one IMU was integrated on a single shank. Due to lack of implementation of a second IMU, the ankle position and velocity on the left and right legs were assumed to be approximately equal in the implementation of the control law. A control law was implemented for each leg separately. For the purpose of testing, the prosthetic feet were clamped to the ground to ensure the system did not topple, which has the potential to damage the hardware. The initial condition was positioned in a crouched configuration with the system at rest (i.e., all joint velocities and accelerations were zero).

Early experiments testing the system showed high-frequency vibration from the motors at roughly 43 Hz. This chattering phenomena resulted in high velocity oscillations at the motor and joints, causing practical issues with direct implementation of the control laws. When a motor began chattering, it would sometimes excite the entire system and the other motors would start showing chatter behavior and could cause significant undesired motion of the entire system, occasionally destabilizing the system. The source of this chatter was likely due to poor controllability of the motors at low speeds. Chatter can be observed when operating one of the motors outside its actuator using a velocity controller, particularly when using high gains. This was the primary contributing factor in determining the limit in the derivative gain penalty in (19) used in the optimization as larger gains tended to exacerbate the chatter issue. To further mitigate this issue, the amplitude of the control signal was decreased for a brief period of time when the acceleration for a joint is beyond a predefined threshold. In addition, friction was added to the system which further reduced the amplitude and occurrences of chatter. These provisions seemed to adequately reduce chatter, allowing for implementation of the control laws.

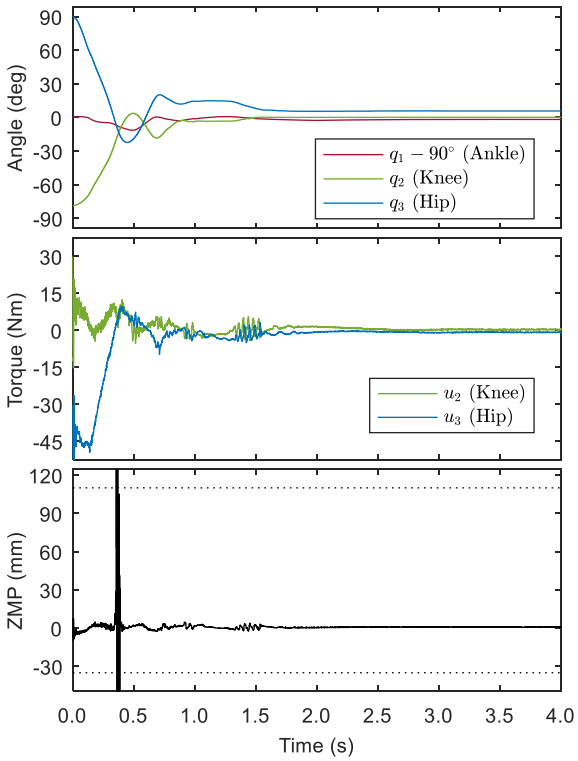

Fig. 13 Experimental results for crouch-to-stand motion using a momentum-based controller

The experimental results of this crouch-to-stand investigation are shown in Fig. 13 for MBC and Fig. 14 for LQR, and both include the response in joint angles, torque inputs, and ZMP. The ZMP was computed based on acceleration calculated from the dynamics model. Both the LQR and MBC were able to bring the system to an upright configuration, where steady-state error was reached after 1.7 s for the MBC and 2.9 s for the LQR. The system settled to 5.8 deg at the hip for MBC and 1.9 deg at the hip for LQR, and smaller values for the ankle and knee joints. The non-zero steady-state value can be explained by the system having uncompensated Coulomb friction and lack of integral action in the controller. Peak torque occurred near the initial condition and was 45.6 Nm at the hip for the LQR and was 59.4 Nm at the hip for MBC. This was significantly larger than the values observed in the simulations from Sect. 4.2. This was likely due to starting from outside the considered initial conditions when determining the region of viability. The ZMP did not exit the support region in the LQR results. However, the ZMP did exit the support region in the MBC results at 0.34 s for approximately 0.05 s. This indicates that, had the prosthetic feet not been clamped to the ground, the system would lose balance at that moment and the bottom of the feet would come off the ground.

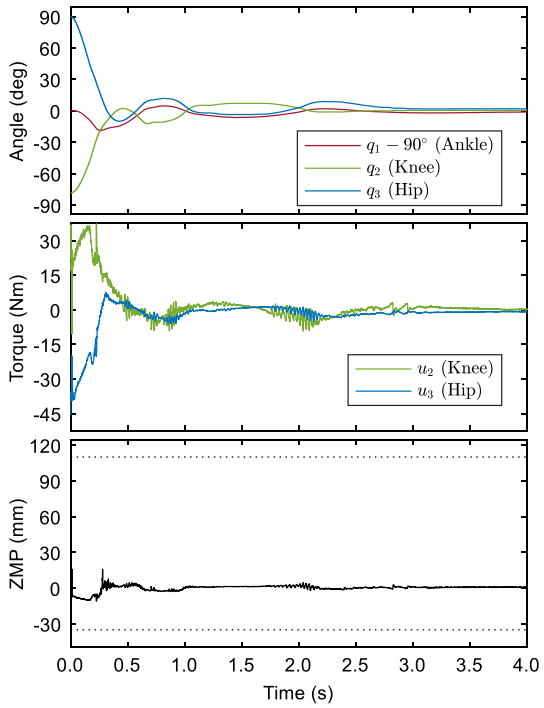

Fig. 14 Experimental results for crouch-to-stand motion using a linear-quadratic regulator

6 Conclusions

This paper presented an extension of the control law proposed by Azad and Featherstone (2016). The revised model-based controller was designed for the purpose of achieving crouch-to-stand motion and control structure is motivated by driving the angular momentum of the system to zero. The momentum-based controller was designed for an under-actuated triple pendulum system where the base joint was uncontrolled, specifically for an orthosis-dummy system in this paper which was actuated at the hip and knee joints. The dynamic model of the system was experimentally determined, and the controller gains were chosen by closed-loop pole placement via numerical optimization. The control law was applied in simulation for a set of balanced initial conditions to determine the system response and region of viability. The simulation results show how a similarly-design linear-quadratic regulator may perform better than the momentum-based controller with regard to response and maximum torque though possibly with an increased risk of knee hyperextension. In addition, the simulation results suggest that linear memoryless state-feedback controllers have the potential for similar performance to the nonlinear momentum-based controller.

Experimental application of the momentum-based controller and linear-quadratic regulator were both successful in bringing the system to a static balanced configuration, thereby validating the feasibility of implementation the control law in hardware. However, the experimental results did not closely resemble the response observed in the simulation results. Upon initial consideration, this can be explained principally due to two reasons. First, the experiment was conducted using an initial condition not considered in the simulations. Second, Coulomb friction in the model used in the simulations may have been underestimated. When adjusting the initial condition in the simulation to match the experimental case and increasing the levels of Coulomb friction in the plant, the simulation results behaved qualitatively more similar to the experimental results when using the linear-quadratic regulator. Interestingly, when using momentum-based controller, the system became unstable in simulation with these adjustments, which was not observed in experiment. In addition, unreported experimental results using the momentum-based controller with an initial condition in a balanced, crouched configuration with the hip and knee joints flexed within the region of viability, the same initial condition from Sect. 4.1, the system sometimes resulted in a large oscillation, primarily at the hip with an amplitude upwards of 30 deg. This was not observed in the simulation shown in Fig. 9. This calls to question the accuracy of the model and the representativeness of the simulations to reality. Although the controllers did successfully drive the system to a balanced, upright configuration in experiment, these concerns limit the generalizability of the reported experimental results.

There are a number of limitations of this work and possible pursuits for future work. First, the simulations may not accurately reflect the behavior of the hardware since the model may be inaccurate. In addition, the effects of chatter from the motors posed practical issues with implementation of the control laws which was resolved to a satisfactory degree with the extemporaneous addition of friction not accounted for in the model. This limits the interpretation of the experimental results for evaluating the viability of the momentum-based control law in general and how it compares to the linear-quadratic regulator when applied outside a simulation context. In addition, hysteresis effects were not considered in the ankle stiffness model, which may be present to some degree from the deformation of the material. Future work warrants resolving these issues for better evaluation of the ability for the control law to bring the system to an upright, balanced configuration. In addition, a clear next step is to perform the experiments without the prosthetic feet of the test dummy clamped to the ground. However, this depends on first having an accurate model for proper balance prediction via zero-moment point analysis in simulation.

Second, analysis of the robustness of the momentum-based controller is not directly considered in the theory. Future work may entail evaluating the effects from modeling inaccuracies or external disturbances. Our recent work (Laubscher and Sawicki 2019b) discusses linear model

uncertainty quantification for a system after feedback linearization, which could be used to assess the degree of unmodeled dynamics. Perturbations can also be applied deliberately in experiment with the addition of weights or external forces to show system robustness.

Third, the numerical optimization used for the closed-loop pole placement problem proved difficult to tune to give reasonable results due to there being many local minima. For the momentum-based controller, a simulated annealing optimization program lessened this issue to give a usable controller, whereas for the linear-quadratic regulator, a more direct approach using a multistart quasi-Newton method was adequate. For the momentum-based controller designed for the double pendulum (Azad and Featherstone 2016), a closed-form solution for the controller gains can be found in terms of a chosen repeated closed-loop pole. Due to the higher dimensionality of the number of controller gains, this is not explicitly possible for the triple pendulum. Further analysis to find a parametric solution for some or all poles could aid by decreasing the dimensionality of the problem. In addition, this could have the effect of relieving some of the difficulty in selection of the objective function used in numerical optimization.

Fourth, the momentum-based control law developed in this paper was designed to drive angular velocities to zero, motivated in part by knowing $L = \ddot{L} = 0$ when $\dot{\boldsymbol{q}} = \boldsymbol{0}$. However, unlike the double pendulum, this is not an if-and-only-if relation. As such, the controller relies on friction in the system to drive it to a static balanced configuration and may explain difficulties encountered in controller synthesis, at least in part. Future work may entail the addition of a third condition to make this biconditional and adding a related term to the controller. This will have the effect of removing the reliance on friction in the system and possibly ease the controller synthesis problem for the momentum-based controller.

Fifth, the simulation results shown in this study suggest that a linear-quadratic regulator may be more suitable for the particular system in this paper than the momentum-based controller. However, this conclusion may not extend to a nominal pendulum system as the stiffness in the prosthetic feet used in this investigation may have significantly aided in the balancing problem. In some preliminary work when developing the controller, not shown here, it was easier to synthesize a momentum-based controller than it was to synthesize a linear-quadratic regulator for the case without ankle stiffness. Future work may include evaluation of the momentum-based controller for a system without any ankle torque, better representing a nominal pendulum system. In addition, future work may entail including the ankle stiffness model in the momentum terms used in the momentum-based controller, which was excluded in this paper as to represent an ideal triple pendulum system.

Appendix 1

When the conditions $L = \dot{L} = \ddot{L} = 0$ are satisfied, a double pendulum will be in a statically balanced configuration as presented in Azad and Featherstone (2016). However, when these conditions are satisfied for the triple pendulum, there may still be motion in the system. This appendix derives the relation between the joint velocities when these conditions are satisfied.

The angular momentum L in (13) and its second derivative $\ddot{L}$ in (14) can be rewritten as a linear combination of the link velocities.

$$\begin{bmatrix} L \\ \ddot{L} \end{bmatrix} = \boldsymbol{M} \begin{bmatrix} \omega_1 \\ \omega_2 \\ \omega_3 \end{bmatrix}$$

$$\boldsymbol{M} = \begin{bmatrix} \Phi_2 + L_1\Phi_3 c_2 + L_1\Phi_5 c_{23} & g\Phi_1 s_1 \\ \Phi_4 + L_1\Phi_3 c_2 + L_2\Phi_5 c_3 & g\Phi_3 s_{12} \\ \Phi_6 + L_1\Phi_5 c_{23} + L_2\Phi_5 c_3 & g\Phi_5 s_{123} \end{bmatrix}^{\mathrm{T}} \tag{27}$$

The nullspace of the matrix $\boldsymbol{M}$ represents the set of link velocities which will result in $L = \ddot{L} = 0$. Since $\boldsymbol{M}$ is a function of the states of the system, the nullspace will be as well. Due to the unwieldy size of the expression, the nullspace is presented only for the upright configuration.

$$\mathrm{null}\left(\boldsymbol{M}|_{\boldsymbol{q}=\boldsymbol{q}_0}\right) = \mathrm{span}\left\{ \begin{bmatrix} n_1 \\ n_2 \\ n_3 \end{bmatrix} \right\}$$

$$\begin{aligned} n_1 &= \Phi_3\Phi_6 - \Phi_4\Phi_5 - L_2\Phi_5^2 + L_2\Phi_3\Phi_5 \\ n_2 &= \Phi_2\Phi_5 - \Phi_1\Phi_6 + L_1\Phi_5^2 \\ &\quad - L_1\Phi_1\Phi_5 - L_2\Phi_1\Phi_5 + L_1\Phi_3\Phi_5 \\ n_3 &= \Phi_1\Phi_4 - \Phi_2\Phi_3 - L_1\Phi_3^2 \\ &\quad + L_1\Phi_1\Phi_3 + L_2\Phi_1\Phi_5 - L_1\Phi_3\Phi_5 \end{aligned} \tag{28}$$

This means link velocities of the form $\omega_1 = \alpha{\cdot}n_1$, $\omega_2 = \alpha{\cdot}n_2$, and $\omega_3 = \alpha{\cdot}n_3$ for any $\alpha \in \mathbb{R}$ will hold true if and only if $L = \ddot{L} = 0$, at least for the upright configuration. For the system in this paper, this gives necessary and sufficient conditions for $L = \ddot{L} = 0$ being joint velocities related by $\dot{q}_2 = -2.3243 \cdot \dot{q}_1$ and $\dot{q}_3 = 1.7993 \cdot \dot{q}_1$.

Appendix 2

The controller is synthesized based on pole placement of the linearized closed-loop system using numerical optimization. The state matrix of this system takes the form

$$\boldsymbol{A} = \begin{bmatrix} \boldsymbol{0} & \boldsymbol{I}_3 \\ \hat{\boldsymbol{K}} & \hat{\boldsymbol{D}} \end{bmatrix}$$

Table 7 Elements of the linearized system state matrix

Element in terms of control parameters	Value	Element in terms of control parameters	Value
$k_{11} = 1403k_{k1} - 2485k_{h1} - 38.44k_h - 1351$	− 513.1	$d_{11} = 106.1k_{k0} + 1403k_{k2} - 188.0k_{h0} - 2485k_{h2} - 0.4074$	387.4
$k_{12} = 797.8k_{k1} - 1413k_{h1} + 21.7k_k + 678.4$	1636.0	$d_{12} = 63.12k_{k0} + 797.8k_{k2} - 111.8k_{h0} - 1413k_{h2} + 26.45$	336.4
$k_{13} = 250.9k_{k1} - 444.5k_{h1} + 213.4$	382.1	$d_{13} = 22.55k_{k0} + 250.9k_{k2} - 39.94k_{h0} - 444.5k_{h2} - 13.1$	171.7
$k_{21} = -3295k_{k1} + 5355k_{h1} + 82.84k_h + 2814$	1007.0	$d_{21} = -249.3k_{k0} - 3295k_{k2} + 405.2k_{h0} + 5355k_{h2} + 0.8486$	− 872.6
$k_{22} = -1874k_{k1} + 3046k_{h1} - 50.97k_k - 1413$	− 3560.0	$d_{22} = -148.2k_{k0} - 1874.0k_{k2} + 240.9k_{h0} + 3046k_{h2} - 57.01$	− 739.2
$k_{23} = -589.4k_{k1} + 958.0k_{h1} - 444.5$	− 808.6	$d_{23} = -52.96k_{k0} - 589.4k_{k2} + 86.08k_{h0} + 958.0k_{h2} + 30.77$	− 365.1
$k_{31} = 2619k_{k1} - 3295k_{h1} - 50.97k_h - 1589$	− 472.8	$d_{31} = 198.2k_{k0} + 2619k_{k2} - 249.3k_{h0} - 3295k_{h2} - 0.491$	618.7
$k_{32} = 1490k_{k1} - 1874k_{h1} + 40.52k_k + 797.8$	2299.0	$d_{32} = 117.8k_{k0} + 1490k_{k2} - 148.2k_{h0} - 1874k_{h2} + 35.08$	485.9
$k_{33} = 468.6k_{k1} - 589.4k_{h1} + 250.9$	475.7	$d_{33} = 42.1k_{k0} + 468.6k_{k2} - 52.96k_{h0} - 589.4k_{h2} - 24.47$	213.8

$$\hat{\boldsymbol{K}} = \begin{bmatrix} k_{11} & k_{12} & k_{13} \\ k_{21} & k_{22} & k_{23} \\ k_{31} & k_{32} & k_{33} \end{bmatrix} \quad \hat{\boldsymbol{D}} = \begin{bmatrix} d_{11} & d_{12} & d_{13} \\ d_{21} & d_{22} & d_{23} \\ d_{31} & d_{32} & d_{33} \end{bmatrix} \tag{29}$$

where $\boldsymbol{I}_3$ is the 3×3 identity matrix and the elements of the matrices $\hat{\boldsymbol{K}}$ and $\hat{\boldsymbol{D}}$ are affine in the control parameters. The full state matrix in terms of system parameters is too large to include in the manuscript. Instead, using the parameters of the system, the elements of the matrices as a function of the MBC gains is provided in Table 7 along with their numerical values for the selected controller.

The eigenvalues of the state matrix from the numerical optimization are -49.60, -44.12, -35.88, -2.792, and $-2.786 \pm 0.2052i$. Since the real components are all strictly negative, the system is locally stable. This means the states will approach the equilibrium point, provided the system configuration and velocities are sufficiently close.

References

Al-Shuka, H. F. N., Corves, B., Zhu, W.-H., & Vanderborght, B. (2016). Multi-level control of zero-moment point-based humanoid biped robots: A review. *Robotica, 34*(11), 2440–2466. https://doi.org/10.1017/S0263574715000107.

Ansari, A., & Murphey, T. (2016). Sequential action control: Closed-form optimal control for nonlinear and nonsmooth systems. *IEEE Transactions on Robotics, 32*(5), 1196–1214. https://doi.org/10.1109/TRO.2016.2596768.

Aphiratsakun, N., & Parnichkun, M. (2009). Balancing control of AIT leg exoskeleton using ZMP based FLC. *International Journal of Advanced Robotic Systems, 6*(4), 34. https://doi.org/10.5772/7250.

Azad, M., & Featherstone, R. (2016). Angular momentum based balance controller for an under-actuated planar robot. *Autonomous Robots, 40*(1), 93–107. https://doi.org/10.1007/s10514-015-9446-z.

Brown, S. C., & Passino, K. M. (1997). Intelligent control for an acrobot. *Journal of Intelligent and Robotic Systems, 18,* 209–248.

Craig, J. J. (2005). *Introduction to robotics: Mechanics and control*. Upper Saddle River: Pearson/Prentice Hall.

Esquenazi, A., Talaty, M., Packel, A., & Saulino, M. (2012). The ReWalk powered exoskeleton to restore ambulatory function to individuals with thoracic-level motor-complete spinal cord injury. *American Journal of Physical Medicine and Rehabilitation, 91*(11), 911–921. https://doi.org/10.1097/PHM.0b013e318269d9a3.

Farris, R. J., Quintero, H. A., & Goldfarb, M. (2011). Preliminary evaluation of a powered lower limb orthosis to aid walking in paraplegic individuals. *IEEE Transactions on Neural Systems and Rehabilitation Engineering, 19*(6), 652–659. https://doi.org/10.1109/TNSRE.2011.2163083.

Fryar, C. D., Gu, Q., & Ogden, C. L. (2012). *Anthropometric reference data for children and adults: United States, 2007–2010* (Vol. 252). Hyattsville, MD: National Center for Health Statistics.

Gui, P., Tang, L., & Mukhopadhyay, S. (2015). MEMS based IMU for tilting measurement: Comparison of complementary and Kalman filter based data fusion. In *2015 IEEE 10th conference on industrial electronics and applications (ICIEA)* (pp. 2004–2009). Presented at the 2015 IEEE 10th conference on industrial electronics and applications (ICIEA), Auckland: IEEE. https://doi.org/10.1109/ICIEA.2015.7334442.

Irfan, S., Mehmood, A., Razzaq, M. T., & Iqbal, J. (2018). Advanced sliding mode control techniques for Inverted Pendulum: Modelling and simulation. *Engineering Science and Technology, an International Journal, 21*(4), 753–759. https://doi.org/10.1016/j.jestch.2018.06.010.

Kwak, N.-S., Müller, K.-R., & Lee, S.-W. (2015). A lower limb exoskeleton control system based on steady state visual evoked potentials. *Journal of Neural Engineering, 12*(5), 056009. https://doi.org/10.1088/1741-2560/12/5/056009.

Laubscher, C. A., Farris, R. J., & Sawicki, J. T. (2017). Design and preliminary evaluation of a powered pediatric lower limb orthosis. In *Proceedings of the ASME 2017 international design engineering technical conferences & computers and information in engineering conference*. Presented at the MR-7 medical & rehabilitation robotics, Cleveland, OH.

Laubscher, C. A., & Sawicki, J. T. (2019a). Gait guidance control for damping of unnatural motion in a powered pediatric lower-limb orthosis. In *IEEE/RAS-EMBS international conference on rehabilitation robotics.* Presented at the IEEE/RAS-EMBS international conference on rehabilitation robotics (ICORR), Toronto, ON, CA.

Laubscher, C. A., & Sawicki, J. T. (2019b). Robust control-oriented modeling of a feedback-linearized powered pediatric lower-limb orthosis. In *ASME international mechanical engineering congress & exposition (IMECE).* Presented at the ASME international mechanical engineering congress & exposition (IMECE), Salt Lake City, Utah.

Rubinstein, R. A., Shelbourne, K. D., VanMeter, C. D., McCarroll, J. R., Rettig, A. C., & Gloyeske, R. L. (1995). Effect on knee stabil-

ity if full hyperextension is restored immediately after autogenous bone-patellar tendon-bone anterior cruciate ligament reconstruction. *The American Journal of Sports Medicine, 23*(3), 365–368. https://doi.org/10.1177/036354659502300321.

Scalera, L., Gasparetto, A., & Zanotto, D. (2020). Design and experimental validation of a 3-DOF underactuated pendulum-like robot. *IEEE/ASME Transactions on Mechatronics, 25*(1), 217–228. https://doi.org/10.1109/TMECH.2019.2947915.

Siciliano, B., & Khatib, O. (2008). *Springer handbook of robotics*. Berlin: Springer.

Spong, M. W., Hutchinson, S., & Vidyasagar, M. (2006). *Robot modeling and control*. Hoboken: Wiley.

Ugurlu, B., Doppmann, C., Hamaya, M., Forni, P., Teramae, T., Noda, T., et al. (2016). Variable ankle stiffness improves balance control: Experiments on a bipedal exoskeleton. *IEEE/ASME Transactions on Mechatronics, 21*(1), 79–87. https://doi.org/10.1109/TMECH.2015.2448932.

Vukobratović, M., & Borovac, B. (2004). Zero-moment point—Thirty five years of its life. *International Journal of Humanoid Robotics, 1*(1), 157–173.

Wang, H. O., Tanaka, K., & Griffin, M. F. (1996). An approach to fuzzy control of nonlinear systems: Stability and design issues. *IEEE Transactions on Fuzzy Systems, 4*(1), 10.

Winter, D. A. (2009). *Biomechanics and motor control of human movement* (4th ed.). Hoboken, NJ: Wiley.

Curt A. Laubscher was born in Cleveland, Ohio, USA, in 1991. He received the B.S. degree in mechanical engineering from Cleveland State University, Cleveland, in 2014. Since 2014, he has been a Graduate Assistant in the Center for Rotating Machinery Dynamics and Control (RoMaDyC) at Cleveland State University while pursuing his doctorate. Since 2012, he has been a student member of the Tau Beta Pi Engineering Honor Society. He is a contributor to a patent for an actuator for a powered pediatric lower-limb exoskeleton. His research interests include robotics, control of dynamical systems, and mechatronics.

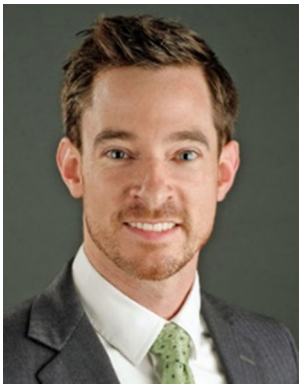

Ryan J. Farris (S'09–M'12) received the B.S. degree in mechanical engineering from Western Kentucky University, Bowling Green, KY, USA, in 2007, and the M.S. and Ph.D. degrees in mechanical engineering from Vanderbilt University, Nashville, TN, USA, in 2009 and 2012, respectively. He is a licensed professional engineer in the states of Tennessee and Ohio. Currently he is the Engineering Manager for Parker Hannifin Corporation's Human Motion and Control Business Unit, Cleveland, OH, USA. He also serves as an adjunct faculty member in the Mechanical Engineering Department, Cleveland State University, Cleveland, OH, USA. His research interests include the design and control of electromechanical devices for medical applications and, in particular, human assistive technologies.

Jerzy T. Sawicki received the M.S. degree in mechanical engineering from the Gdansk University of Technology, Gdansk, Poland, in 1980, the M.S. degree in applied mathematics from the University of Gdansk, Gdansk, in 1986, and the Ph.D. degree in mechanical engineering from Case Western Reserve University, Cleveland, OH, USA, in 1992. He has published more than 250 peer-reviewed papers in the fields of rotor dynamics, tribology, dynamics and vibrations, and advanced control. Dr. Sawicki is the Bently and Muszynska Endowed Chair and Professor and Director of the Center for Rotating Machinery Dynamics and Control (RoMaDyC), Washkewicz College of Engineering, Cleveland State University. He also serves as the Vice President for Research at Cleveland State University.